Journal of Power Sources 524 (2022) 231063

Contents lists available at ScienceDirect

Journal of Power Sources

journal homepage: www.elsevier.com/locate/jpowsour

X-ray imaging and micro-spectroscopy unravel the role of zincate and zinc oxide in the cycling of zinc anodes in mildly acidic aqueous electrolytes

Majid Kazemian [a], Francesca Rossi [b], Andrea Casaroli [c], Tommaso Caielli [d], Burkhard Kaulich [a], Maya Kiskinova [e], Ivonne Sgura [f], Benedetto Bozzini [d,*]

[a] Diamond Light Source Ltd., Harwell Science and Innovation Campus, OX11 0DE, Didcot, Oxfordshire, UK
[b] Department of Innovation Engineering, University of Salento, via Monteroni, 73100, Lecce, Italy
[c] Department of Mechanics, Politecnico di Milano, via la Masa 1, 20156, Milano, Italy
[d] Department of Energy, Politecnico di Milano, via Lambruschini 4, 20156, Milano, Italy
[e] Elettra – Sincrotrone Trieste S.C.p.A., S.S. 14-km 163.5 in Area Science Park, 34149, Basovizza, Trieste, Italy
[f] Department of Mathematics and Physics, University of Salento, via per Arnesano, 73100, Lecce, Italy

HIGHLIGHTS

- Soft X-ray absorption spectromicroscopy (XAS) gives insight for Zn electrochemistry.
- Zn anode cycling in mildly acidic aqueous electrolyte can generate zincates.
- Parasitic HER yields space distribution of Zn species in mildly acidic electrolyte.
- Chemical-state distribution of discharged and cycled Zn anodes, disclosed by XAS.
- Homogeneous primary current distribution cannot avoid mesoscopic heterogeneities.

GRAPHICAL ABSTRACT

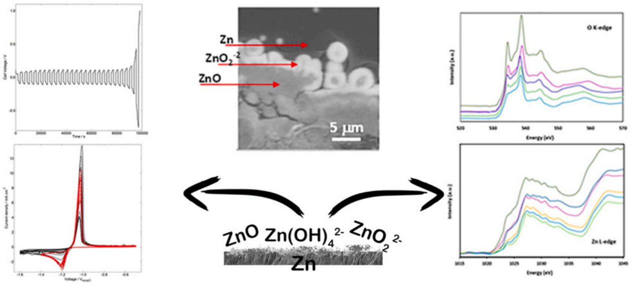

ARTICLE INFO

Keywords:
Zn anode
Mildly acidic
Zincate
X-ray absorption spectroscopy
STXM
Hyperspectral mapping

ABSTRACT

Sustainability, environmental and safety concerns raised by the increasing demand of batteries are driving research towards post-lithium technologies. Rechargeable Zn batteries are strong candidates, but still not practically viable, owing to the extensively studied, but poorly understood unstable behavior of Zn metal upon discharge-charge cycling. This limiting factor warrants more fundamental investigations and the present report provides the lacking molecular-level information on the Zn-based compounds forming at the electrode/electrolyte interface as a result of electrochemical cyclic in weakly acidic aqueous electrolyte. The results are obtained using *ex situ* X-ray absorption spectromicroscopy maps, modelled mathematically and complemented with cyclic voltammetry, symmetric-cell tests and electron microscopy. We have identified the role of the zincate precipitation resulting from local alkalinization during recharge, combined with additional zincate formation and decomposition to zinc oxide during discharge. The mathematical model allowed a transparent interpretation of morphochemical changes observed. The synergy of these processes leads to electrochemical localization effects, resulting in the formation of a complexly structured and low conductive ZnO-based template, that might play a role in driving shape changes.

---

* Corresponding author.
E-mail address: benedetto.bozzini@polimi.it (B. Bozzini).

https://doi.org/10.1016/j.jpowsour.2022.231063
Received 14 October 2021; Received in revised form 19 December 2021; Accepted 20 January 2022

1. Introduction

On September 2020, the European Commission proposed to reduce by 2030 the net greenhouse gas emissions to at least 55% of the 1990 level [1]. In order to achieve this goal, a large proportion of activities contributing to CO_2 emissions must be converted into clean and sustainable analogues. Concerning energy production, the scientific and industrial communities are struggling for the development of large scale, safe and low-cost systems that could efficiently store and regulate the intermittent energy of the renewable resources [2,3]. Due to their ability to convert chemical into electrical energy and vice-versa, rechargeable batteries are the best candidates. Lithium-ion batteries (LIBs) have been extensively used in the field of portable electronics and electric vehicles in the last two decades. However, LIBs do not appear the best choice for renewable energy storage, owing to: (i) their low power density, which prevents to be highly responsive to the perturbations affecting the power grid [4], and (ii) their limited lifetime [5]. In addition, safety and high-cost issues impede the large scale implementation of LIBs [6]. One of the viable alternatives can be the next-generation Zn-based batteries with Zn-air, Zn-bromine, Zn-cerium and Zn–MnO_2 systems in the foreground. In fact, Zn is abundant (about 1.9 billion tons worldwide) [7], inexpensive (~US\$2.4 kg^{-1} vs US\$19.2 kg^{-1} of Li) [6], stable in aqueous solutions and exhibits high gravimetric (820 $mAhg^{-1}$) and volumetric (5855 $mAhL^{-1}$) theoretical capacities [7]. However, rechargeable batteries with Zn anodes are still far from large-scale commercialization due to their low cyclability. Specifically, the performance of the Zn anode in alkaline devices is affected by the following drawbacks: (i) corrosion, due to parasitic hydrogen evolution; (ii) passivation during the discharge process, due to the formation of zincates in solution; (iii) shape changes and (iv) dendrite growth during recharge, owing to still poorly understood localization and electro-crystallization issues [8–11]. Among the vast investigations of secondary Zn-based battery chemistries in the last decade, the re-emerged results on a mildly acidic Zn–MnO_2 cell, reported by Yamamoto et al. [12], have led to renewed interest. The observed exceptional cyclability of the Zn anode in a mild acidic aqueous electrolyte has attracted the interest of the energy community in the rechargeable aqueous zinc ion batteries (AZIBs). In fact, as demonstrated by the Pourbaix diagram, under mildly acidic conditions (pH = 4-6), the stripping/plating reactions follow a direct path, favouring the charging process and hindering the anode passivation and the shape alterations of the active material [4,13]. Nevertheless, self-discharge and dendrite growth still remain an open issue, leading to practical limitations of the plating/stripping current efficiency. Notwithstanding the growing number of publications on cathode chemistry and laboratory battery tests [4], still the electrochemical and morphological behaviour of the zinc anode in mildly acidic ambient is not well understood. It is commonly agreed that, considering the performance-cost ratio, the aqueous $ZnSO_4$ solutions are among the best candidates [14,15]. In fact, using this electrolyte, the galvanostatic charge/discharge cycles (GCD) in Zn symmetrical cells show an increase of the cell lifetime of the order of ~100 h, compared to the alkaline systems for a given DOD [16]. Furthermore, the electrodeposition of metallic Zn in weakly acidic solution, proceeds via the formation of stacked hexagonal-like crystalline structures rather than the sharp tree-like structures typical of the alkaline systems [17]. Nevertheless, the formation of dead Zn due to the breakage of these stacked structures and the formation of basic salts, often described as $Zn_4(OH)_6SO_4$ [13], limit the utilization of the Zn ion in this electrolyte. Triflate-based electrolytes are reported to show better performance, due to the bulky anions limiting the Zn ion solvation, thus increasing the plating/stripping efficiency, but they are expensive, difficult to source and also promote the formation of stacked structures that can produce dead material [15,18]. Other salts, such as $Zn(ClO_4)_2$ and $Zn(NO_3)_2$, are not suitable for battery applications, owing to their low electrochemical stability in the potential range of interest, due to the strong oxidizing properties of ClO_4^- and NO_3^-, as demonstrated by Zhang et al. [15]. Beyond the choice of a suitable electrolyte, several strategies can be implemented in order to enhance the stripping/plating efficiency and to minimize the formation of outgrowth morphologies. Specifically, instead of classical glass fibre separator, polymeric ion-exchange membranes can be exploited to improve the ion mass transport [19], cationic organic additives can be added in the electrolyte to regulate the initial nuclei formation and inhibit the following dendrite growth [20] and the anodes can be functionalized either by sputtering the Zn surface with some noble metals (i.e. gold nanoparticles [21]) or by the fabrication of tailor-made host structures [21]. The success of the proposed mitigation strategies, summarised above, is still limited by the scanty insight into the electrochemistry and interfacial chemistry of the Zn anodes in mildly acidic aqueous ambient, and their evolution during cycling. This paper is a step forward to shed more light on these aspects, through a systematic investigation of Zn anodes in sulphate electrolytes, combining electrochemical measurements with *ex situ* X-ray imaging and absorption micro-spectroscopy, accompanied by mathematical modelling of the electrochemical phase-formation processes. The access to elemental and chemical-state distribution of Zn and O with sub-micrometric spatial resolution has provided very important information about the surface chemistry and space organization resultant from the electrochemical conditions. Mathematical modelling allowed to interpret the formation of spatial inhomogeneity within a clear physico-chemical framework. It should be noted some studies of Zn battery anode materials have appeared, that use X-ray absorption spectroscopy (XAS), though without spatial resolution [22–25], mainly focussing on properties such as crystalline structures, density of states etc. Adding spatial resolution to XAS notably increases its power, enabling the exploration of the nature and lateral collocation of reaction products that can correlated with shape changes. This study is focused on the role of basic salt precipitation and nature in cathodic and anodic processes during anodic/cathodic cycling for providing firm background to further rational studies of anode surface modifications or electrolyte engineering.

2. Experimental

2.1. Materials

In the electrochemical measurements and treatments, the electrolyte consisted of supporting electrolyte - an aqueous solution of 0.5 M Na_2SO_4 (Sigma-Aldrich) -, to which 10 mM $ZnSO_4$ (Sigma-Aldrich) was added, according to the experimental requirements (see Section 2.2). For galvanostatic charge/discharge cycles in symmetrical Zn/Zn cells, the electrolyte was an aqueous solution of 2 M $ZnSO_4$ (Sigma-Aldrich). Milli-Q water was employed as the solvent.

Thin films of Zn (thickness150 nm) and ZnO (thickness 300 nm) were sputter-deposited on 75 nm Si_3N_4 windows of 500 μm^2 (Silson Ltd. UK) in the Nanofabrication Facility at the University of Bath. The pristine samples were homogeneous in-plane down to the scale of a few tents of nanometres. Zincate-rich standard samples (henceforward denominated “zincate standards”, for simplicity) were obtained by filtration of the precipitate obtained by dissolving electrochemically Zn in 6 M KOH solutions.

2.2. Electrochemical measurements

2.2.1. Cyclic voltammetry (CV)

CVs were performed in a standard three-electrode cell (AMEL 497 Universal Cell), with an Ag/AgCl 3 M KCl reference electrode (AMEL 373/SSG/12), two identical platinum counter electrodes (AMEL 805/SPG/12), placed symmetrically with respect to the working electrode (WE) and reference electrode (RE) to improve the uniformity of the current distribution and reduce ohmic losses. All potentials in this work are referenced to the Ag/AgCl 3 M KCl electrode. A glassy carbon (GC) electrode (AMEL 492/GC/3) with a surface area of 0.07 cm^2 was employed as WE. The cell contained 30 ml of electrolyte (see Section 2.1

for the composition), which was degassed by N_2 bubbling (0.5 nlt/min) before running the experiment and kept under a blanket of flowing N_2 during the electrochemical measurements. CVs were performed with a 3F VersaSTAT potentiostat/galvanostat at 25 mV s^{-1}, in relevant potential ranges that will be specified. All CV measurements were repeated three times, in order to assess the reproducibility of the system. Specifically, before each experiment, the electrode was immersed in 70% nitric acid for a few seconds, rinsed with DI water, gently polished with 2500 grinding paper and finally sonicated for 5 min in DI water. To ensure complete removal of zinc compounds, the Pt CEs were washed with 10% nitric acid and accurately rinsed with DI water. The RE and all the cell components were thoroughly washed with DI water. All components and electrodes were finally rinsed with Milli-Q water. The CVs were performed with the following protocol: (i) The cleaned GC electrode was subjected to CV cycling (5 cycles in range $0.5 \div -1.8$V, starting from the open-circuit potential (OCP)) in the pure supporting electrolyte (see Section 2.1) to positively assess the WE condition. (ii) $ZnSO_4$ was added to the electrolyte, then a second CV was performed: 10 cycles from -0.5 to -1.6V, starting from anodic terminal potential. In special cases other terminal potentials have been selected, as specified in the relevant section of the paper. The cathodic current efficiency was evaluated gravimetrically by galvanostatic electrodeposition of Zn films, in a current density (CD) range of interest for battery applications [26], onto carbon-steel foils for a nominal weight gain of 2.5 mg/cm^2. Three samples were electrodeposited at each CD, using a fresh aliquot of electrolyte. Care was taken to avoid loss of electrodeposit from samples grown in the low-CD range, leading to mossy deposits. After electrodeposition and gentle, but thorough rinsing with Milli-Q water, before weighting, the samples were vacuum-dried overnight at 40 °C with a VT 6060 M oven and cooled *in vacuo* to room temperature.

2.2.2. Galvanostatic charge/discharge cycles (GCD) -

Symmetrical Zn/Zn cells were assembled using an EL-CELL ECC-AIR-NI split cell, reproducing the geometry of a 2032 coin cell, in which the electrodes are mounted in horizontal position. The electrodes consisted of two Zn discs (99.98% Alfa Aesar, 0.25 mm thick and 18 mm diameter) as-rolled, that were degreased with acetone, rinsed with Milli-Q water and put in contact with two austenitic stainless steel (AISI 304) current collectors (18 mm diameter, 0.6 mm thick). The electrodes were kept separated by an O-ring and the cell was filled with 300 μl of electrolyte. GCD cycles were performed at 1 mA cm^{-2} with 60 min periods (30 min positive and 30 min negative current). Each GCD cycle was run until the cell potential reached a cut-off of ±1 V, corresponding to experiment termination by passivation.

2.2.3. Preparation of samples for ex situ X-ray absorption microspectroscopy

Zn and ZnO membranes were subjected to galvanostatic polarization sequences at 1 mA cm^{-2}, specified in Section 3.3, in 0.5 M Na_2SO_4 electrolyte using a standard two-electrode electrochemical cell with a Pt CE. The WE was immersed in the electrolyte, and electrical contact was placed in the middle of one of the square WE sides, at 1 mm from the optical window, with a Ni clamp. The electrode arrangement in the cell (see Refs. [27–30] for computational details referring to electrodes of similar geometry) and the resistivity of the layers [31,32] ensure a homogeneous secondary current density distribution at the analysed positions.

2.3. Scanning X-ray absorption micro-spectroscopy (μ-XAS)

2.3.1. μ-XAS instrumentation

The XAS spectra and images reported in this work were acquired in transmission, using the I08-SXM beamline at Diamond Light Source Ltd., Didcot, UK. This beamline hosts two endstations: I08 - Scanning X-ray Microscope (SXM) with multimodal detection capabilities [33] and I08-1 - X-ray Ptychography. The I08-SXM uses as photon source an Apple II type undulator covering the 250–4400 eV energy range. The nanoprobe is formed by a Fresnel zoneplate and the sample is raster-scanned in the focal plane for obtaining images. SXM is quite versatile and, by using appropriate detectors, allows simultaneous recording of transmitted X-rays, emitted photons and electrons. In the present experiment, a photodiode was used for data acquisition in transmission mode. The μ-XAS spectra are extracted from the stack of images recorded with 0.1 eV energy steps in the energy windows across Zn L-edge (1020–1040eV) and O K-edge (525–555eV), respectively. The spatial resolution down to ~50 nm was achieved with proper optics setting.

2.3.2. μ-XAS data processing

μ-XAS results were elaborated in view of: (i) assessing the spectral components revealing the Zn and O chemical-state under different electrochemical conditions of the Zn-based electrodes and (ii) assigning the corresponding space distributions. Appropriate fitting procedures were defined and implemented in the elaboration of the hyperspectral images, in order to extract chemical-state distribution maps. For getting chemical-state maps, we employed background-subtracted and normalized spectra and plotted the relative intensities corresponding to the diagnostic energies discussed in the following two subsections, using the MANTiS software program [34].

Finally, XAS maps have been modelled mathematically, carrying out parameter identification by comparing their morphologies with the solutions of the DIB reaction-diffusion PDE model for electrochemical phase formation, the physico-chemical foundations of which are expounded in detail in Ref. [35]. In Ref. [36], the authors have shown that, in different regions of the parameter space, this model entails a rich spatio-temporal distribution of pattern solutions, that can be classified into two main types: (i) structured stationary Turing patterns and (ii) unstructured Turing-Hopf dynamic patterns [37]. Parameter identification for the DIB model for experimental hyperspectral maps, has been recently carried out by the authors for XRF [38], XPS [39] and XAS [40] data. The XAS maps of this work can be modelled with parameters in the Turing-Hopf region, specifically in the neighbourhood of a codimension-two Turing–Hopf (TH) bifurcation point in the (C,B) variety of the parameter space. Parameters C and B account for electrochemical adsorption and inhibition of electrodeposition by adsorbates, respectively: extensive details are provided in Refs. [35,39]. Here, we have solved the DIB model by the ADI-ECDF numerical method based on a finite difference spatial discretization, described in detail in Refs. [37,38], on a square domain $\Omega = [0,L_x] \text{ x } [0,L_x]$, $L_x = 200$, with timestep $h_t = 5 \times 10^{-4}$. The spatial discretization is given by the pixel size of the image Z to be fitted, then Z is treated as a $N \times N$ matrix (in grayscale). If Θ is the numerical solution for the chemistry variable of the DIB model, standing oscillations of the spatial mean $<\Theta(t)>$ are used as an indicator that the limit cycle has been attained at the final time T. Then we choose for numerical integration the time interval [0,T], T = 4. Hence, the fitted maps reported are the patterns at the final time T, identified among a set of several simulations obtained by varying the parameters $\mathbf{p}$=(C,B) in the Turing-Hopf zone. The optimal simulated maps and the corresponding optimal parameter couples $\mathbf{p}^*$=(C*,B*) are those yielding the minimum values of the relative error in Frobenius norm given by $E_F(\mathbf{p}) = ||Z - \Theta(\mathbf{p})'||/||Z||$, where Z is the original experimental image normalized and Θ' the normalization of the numerical solution Θ. More details on the optimization procedure are provided in Ref. [38]. Confidence intervals for the parameter estimates are evaluated by computing the range in which the Frobenius error changes by less than 5% with respect to the minimum identified.

3. Results and discussion

In this work we have endeavoured to reveal the impact of electrochemical polarization on the interfacial chemistry of Zn and, in particular, on the coupled irreversible changes in morphology and chemical-

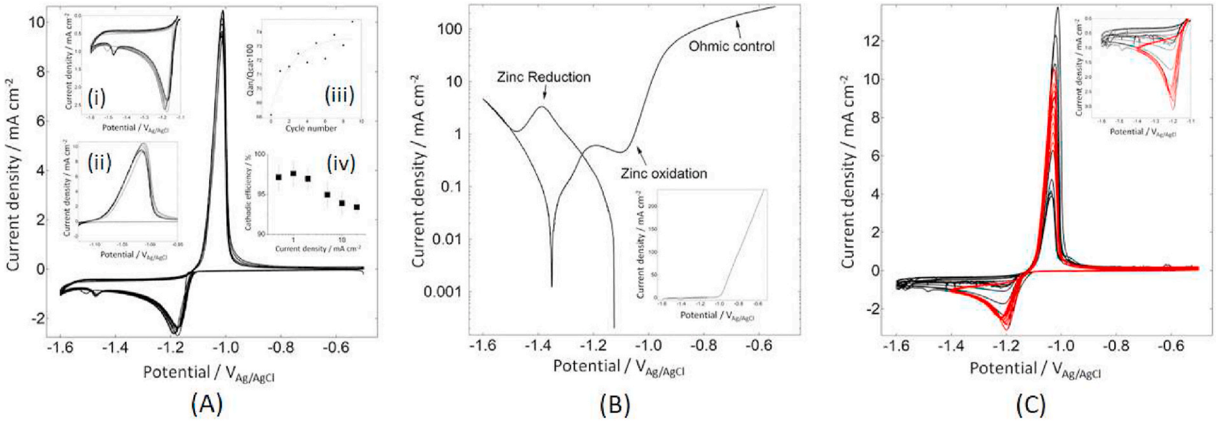

Fig. 1. A) Cyclic voltammograms (CVs) recorded with a glassy carbon electrode in contact with a 0.5 M $NaSO_4$ + 10 mM $ZnSO_4$ aqueous solution. Number of cycles: 10. Scan rate 25 mV s^{-1}. Insets (i) and (ii): expanded cathodic and anodic ranges, respectively. Inset (iii): ratio of anodic and cathodic charges computed from the CVs of Fig. 1A, as a function of the cycle number. Inset (iv): cathodic current efficiency. B) Linear sweep voltammogram with potential inversion, recorded with a Zn rod electrode in contact with a 0.5 M $NaSO_4$ + 10 mM $ZnSO_4$ aqueous solution. Experiment started at OCP, then potential ramped to the cathodic terminal potential (CTP), after which the potential was scanned to the anodic terminal potential. Scan rate 25 mV s^{-1}. Inset: same voltammogram on linear scale. C) Cyclic voltammograms recorded with a glassy carbon electrode in contact with a 0.5 M $NaSO_4$ + 10 mM $ZnSO_4$ aqueous solution, with different cathodic terminal voltages (black and red plots). Total number of cycles: 500, of which we show one every 50. Scan rate 25 mV s^{-1}. (For interpretation of the references to colour in this figure legend, the reader is referred to the Web version of this article.)

state distribution. These changes correlate with the buildup of isoluble species, resulting from the alternation of anodic and cathodic condition. To this aim, we performed several types of experiments: (i) electroanalytical measurements spanning the cathodic and anodic ranges (Section 3.1); (ii) imaging *post mortem* the electrodes after cycling symmetric coin-cell type devices (Section 3.2) and (iii) *ex situ* μ-XAS of electrodes subjected to characteristic battery conditions. Moreover, we have mathematically modelled XAS maps, with the approach described in Section 2.3.2. We decided to operate *ex situ* in order to have better control on prolonged cycling conditions. This is an important starting point for the future ageing studies with microfluidic cells we are developing based on our experience for *in situ* spectromicroscopy with a sealed cell [41,42].

3.1. Cyclic voltammetry

Fig. 1A reports one typical instance of the 18 replicated CVs (10 cycles) measured in the additive-free electrolyte in order to achieve a thorough grasp on instrumental and reproducibility issues. The results from these measurements are in excellent quantitative matching, with a well-defined and controlled deviation of the current values, which was always below 15%. The cathodic deposition of Zn (Inset (i) of Fig. 1A.) starts at ca. −1.15 V in the first cycle, in which Zn nucleation occurs at the bare glassy-carbon surface, and at ca. −1.10 V in the following ones, in which Zn nucleates in the presence of a film or residual corrosion products. After an initial current-density growth that follows the I–V dependence described by the Butler-Volmer equation, a mass-transport controlled peak forms, with a maximum at ca. −1.17 V. The limiting CD under stagnant conditions is attained during the anodic-going scan, as one can appreciate from the plateau extending in the range ca. −1.5÷-1.3 V. At high cathodic potentials, close to −1.5 V, an additional peak can be observed, that can be explained with the reduction of zinc oxides/hydroxides, forming in the catholyte owing to local alkalinization brought about by HER concomitant with Zn electrodeposition. This process in well-known in electroplating (e.g. [43]), and it can be so extensive that it also affects the performance of acidic metal-plating baths, but it has received limited attention in the case of Zn anode recharge in mildly acidic aqueous battery electrolytes. HER during Zn electrodeposition is also witnessed by a cathodic current efficiency that is slightly, but measurably lower than 100% (Fig. 1A, Inset (iv)). It can be noticed that the current densities in the whole cathodic loop tend to decrease with the number of CV cycles, owing to the accumulation of oxidation products that can neither be fully solubilized in the anodic interval, nor completely reduced in the cathodic period.

The anodic range of the CVs (Inset (ii) of Fig. 1A) is dominated by the stripping of Zn deposited in the cathodic range, and exhibits a prominent peak, followed by a sharp decrease and terminating with a low CD tail extending for some tens of mV. Since in mildly acidic electrolytes the tendency to passivation is weak, the potential range of the peak in which the slope of the I–V curve is negative is dominated by Zn consumption rather than by oxide formation, as in alkaline solution. Evaluation of the anodic-cathodic charge ratios (Inset (iii) of Fig. 1A.) over all cycles of all replicated runs confirms this view. To confirm experimentally the negligible propensity of Zn to passivate under these conditions of electrolyte and cell geometry, we repeated the measurement with a Zn rod as WE: the results are shown in Fig. 1B and evidently confirm active corrosion (in fact, under ohmic control) over the whole investigated potential range.

Notwithstanding dominating active corrosion, the residual CD tail observed in the CVs measured with a glassy-carbon electrode, can be justified with the formation of Zn(II)-containing species, imparting some degree of pseudo-passivation, impeding the completion of Zn stripping, and forming a compact and hard-to solubilize layer of corrosion products, favoured by the presence of an inert electrode material. The progressive decrease of the CD values, already noted in the cathodic loop and confirmed in the anodic one, is fully compatible with the buildup of an anodic film over cycling.

To further investigate the alkalinization of the catholyte resulting from the application of cathodic potential, and anodic pseudo-passivation processes occurring during the operation of Zn anodes in a near-neutral aqueous electrolyte, we carried out prolonged voltammetric cycling (500 scans, Fig. 1C) and assessed the effect of shifting the CTP from −1.6 (black plot) to −1.4 V (red plot). It is worth nothing that after 500 cycles with both CTPs, the WE was covered with an evident white layer – that we did not investigate further –, that was clearly thicker after the experiment with CTP of −1.6 V. The results in Fig. 1C indicate that, coherently with the CVs of Fig. 1A and irrespective of the CTP, there is a progressive decrease of CD in both the cathodic and anodic ranges. A closer look at the CVs in the cathodic range (Inset of Fig. 1C) reveals that, while with a CTP of −1.4 V the limiting CD is not affected by cycling, the rising portion of the cathodic CD before the mass-transport control peak is systematically lowered, though not as

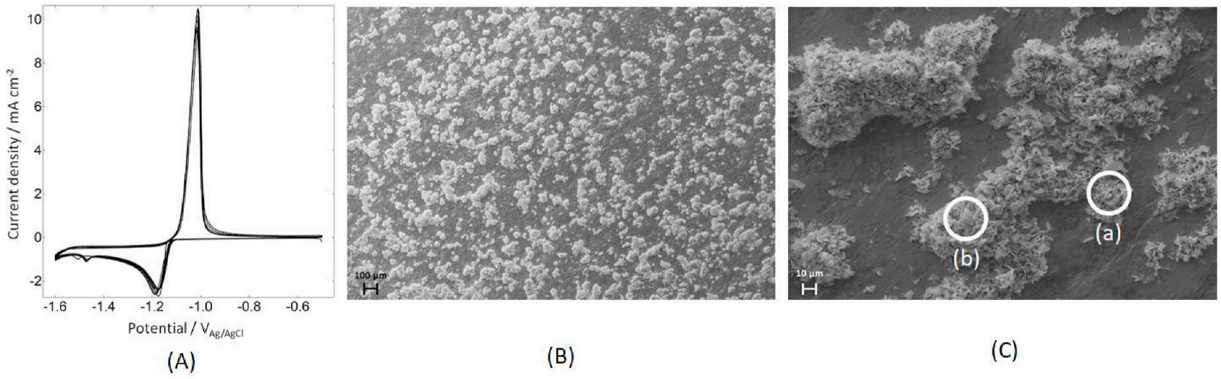

Fig. 2. A) GCD cell potential profile at Zn/Zn symmetrical split cell run at 1 mA cm^{-2}. The cell contains a free electrolyte 2 M ZnSO4. B) and C) SEM images of the Zn electrodes cycled in a Zn/Zn symmetrical cell at 1 mA cm^{-2} in 2 M $ZnSO_4$ for ca. 98000 s.

much as with the CTP set at −1.6 V. The relative variations of consumed charge reveal that the cathodic charge is systematically higher (in the range ca. 10 ÷ 40%) than the anodic one: in principle a difference between the anodic and cathodic consumed charges can be due to HER and to the formation of Zn-containing species, that cannot be solubilized anodically and impede the complete stripping of the deposited zinc. The cathodic current efficiency data reported in Inset (iv) of Fig. 1A confirm this view. HER thus leads to the fact that the trend of Fig. 1C is dominated by the build-up of an insoluble film, which impedes the completion of Zn dissolution. Mechanistically, this scenario is compatible with the anodic formation of type II oxides, as well as with the cathodic precipitation of zinc basic salts, resulting from the alkalinization of the catholyte and favoured by a CTP of −1.6 V: the presence of both species has been demonstrated in neutral environment by quasi-*in situ* XAFS, recently performed in our group and in a 1 M $ZnSO_4$ electrolyte by Cachet [44]. Indeed, both processes tend to reduce the active area of the electrode and, in addition, can also give rise to a porous layer of type-I oxide [45], that also hinders mass transfer. Another piece of evidence hinting at the occurrence of the cathodic precipitation process is that, with the CTP set at −1.6 V, after ca. 100 cycles, random c.d. spikes can be observed both in the cathodic and anodic ranges, that are characteristic of pseudo-passivation conditions.

3.2. *Galvanostatic charge-discharge cycling of Zn/Zn symmetrical cell*

Fig. 2A shows the potential profile of the experiment run at 1 mA cm^{-2} in 2 M $ZnSO_4$. The shapes of the potential transients can be qualitatively illustrated in terms of cathodic and anodic metal electrochemistry: a full discussion of this topic can be found in Ref. [46]. In particular, the first half-cycle in Fig. 2A shows an initial high value of the cell potential, followed by a fast decrease which immediately reaches a constant value: this behaviour is indicative of the presence of a nucleation process, followed by the growth of a Zn film of increasing surface area, combined with ohmic contributions. The remaining portion of the potential profile is characterized by half-cycles exhibiting a continuous increase of the cell overpotential, which indicates the occurrence of gradual passivation that causes the failure of the cell at ca. 98000 s.

Fig. 2B and C represent the morphological analysis of the Zn electrodes cycled in the experiment illustrated in Section 3.1.2, where uniform dispersion of Zn agglomerates is evident all over the Zn surface (see Fig. 2B). In particular, each agglomerate is composed by a mixture of hexagonal-like crystallites, typical of Zn electrodeposits obtained in mildly acidic baths (features (a) in Fig. 2C) [47,48] and ZnO platelets (features (b)) [49].

3.3. *μ-XAS and imaging*

The XAS maps of the electrodes subjected to representative electrochemical conditions (detailed below, and coded A, B and C) evidenced clearly the induced inhomogeneity accompanying the changes of Zn chemical states. The obtained information is based on the corresponding Zn L-edge and O K-edge μ-XAS, encoding the chemical speciation variations of the initially homogeneous Zn anode as a result of the discharge-charge cycles. Specifically, we selected the following cases, that are exemplary of battery operation and provide reasonable coverage of the

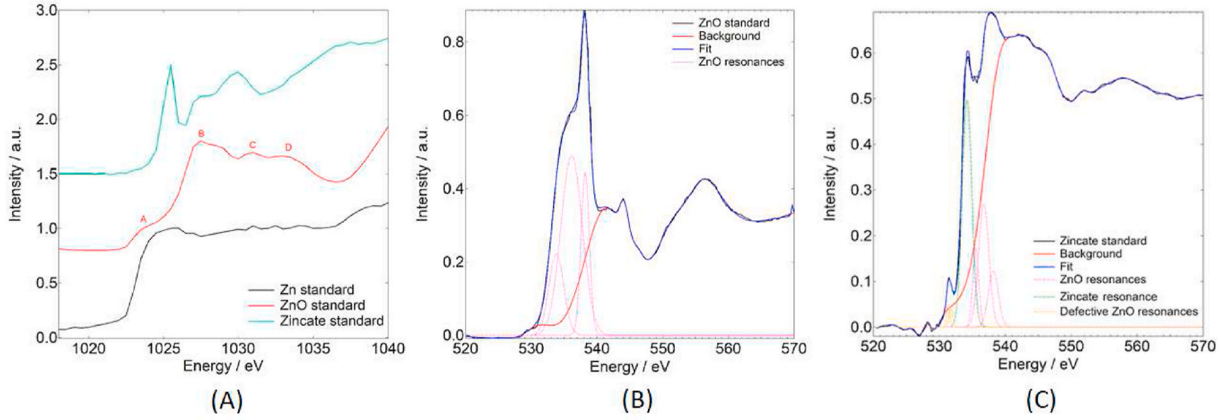

Fig. 3. A) Zn L-edge XAS spectra of the Zn (black line), ZnO (red line) and zincate (green line) standards. O K-edge XAS spectra of: B) ZnO standard sample, C) zincate standard sample. See text for details on fitting. (For interpretation of the references to colour in this figure legend, the reader is referred to the Web version of this article.)

Table 1
Electronic transitions occurring at the Zn L-edge and the O K-edge.

Zn L-edge energy position (eV)	Transition
A – 1023.5	Dipole-forbidden transitions [55] 2p → 4s [52] 2p → 4p4d [51,53,54]
B – 1027.5 C – 1031 D – 1033	2p → 4d, d-d interactions of the 4d orbitals, O 2p-hybridized band [51–55]
O K-edge energy ranges (eV)	Transition
530–540	1s → O 2p hybridized Zn 4s [23,25,51–53,58]
540–550	1s → O 2p hybridized Zn 4p and 4d [23,25,51–53,58]
550–570	1s → O 2p – Zn 4d mixed states [23,25,51–53,58]

range of practically relevant conditions [50]: (A) oxidation at +1 mA cm^{-2} of a pure Zn layer (A1: weak oxidation, 1 min corresponding to DOD of ca. 12% and A2: deep oxidation, 5 min corresponding to DOD ca. 60%), characteristic of almost discharged anode, (B) reduction of a pure ZnO layer at −1 mA cm^{-2} for 4 min (charge leading to a nominal DOD ca. 44%), characteristic of a fully oxidized anode or of the initial state of a fabricated discharged battery and (C) reduction-oxidation cycling of an initially pure ZnO layer (10 cycles ±1 mA cm^{-2} for 4 min, DOD ca. 44%, terminated cathodically).

3.3.1. Zn L-edge and O K-edge μ-XAS

Due to lack of previous Zn L-edge XAS measurements for the zincate and metallic Zn standard samples, we first performed Zn L-edge and O K-edge XAS measurements of standard Zn, ZnO and zincate-rich samples, shown in Fig. 3. It should be noted that the presence of small fractions of ZnO, in the zincate standard, is expected owing both to the poorly known dehydration equilibria in solution and the electrochemical formation of ZnO nanoparticles [51]. This was taken into account by appropriate numerical correction, derived from the elaboration of precipitate samples from different batches; more details on the chemistry of precipitates from electrochemical dissolution of Zn will be provided in a dedicated paper. Since the Zn ion in ZnO is in 3 d^{10} state, the Zn L-edge XAS spectra provide information about the electronic transitions from 2p to 4s, 4p and 4d lowest unoccupied states, obeying the dipole-transition selection rule. All authors [52–56] agree on the assignment of the features present in the 1020–1040 eV energy range to the transitions involving the 4p and 4d orbitals, with the exception of [53,56] that associate the lowest energy feature A with the 2p→4s transition and with dipole-forbidden transitions.

O K-edge XAS, probes the O 2p unoccupied states in the conduction

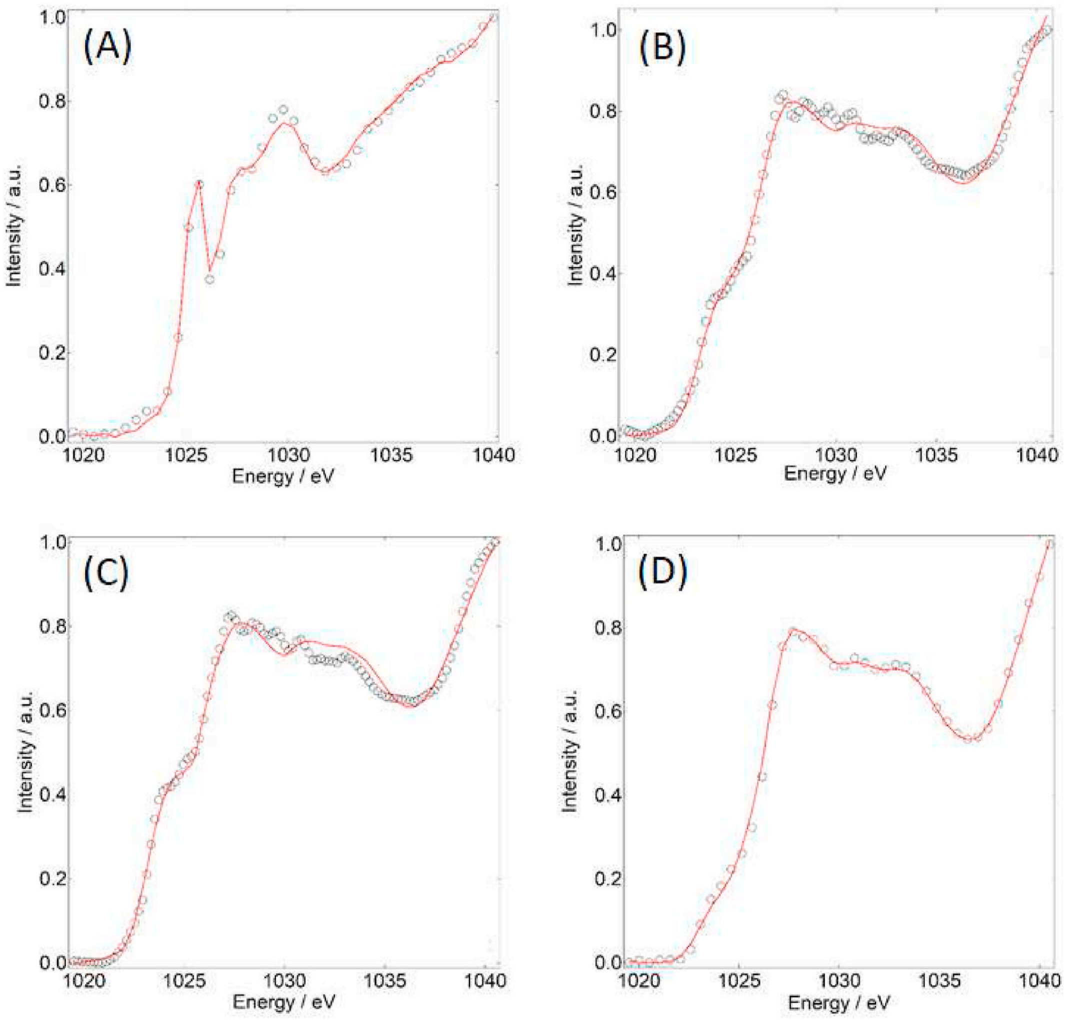

Fig. 4. Zn L-edge XAS spectra (circles: experimental data, red plot: fit) of: A) Zn electrode after discharge (condition A2, region of spheroidal features in Fig. 5B). B) and C) ZnO electrode after application of single charge electrochemical polarization (condition B, regions with different Zn metal content in Fig. 6. D) ZnO electrode, after electrochemical cycling, terminated in charged state (condition C). (For interpretation of the references to colour in this figure legend, the reader is referred to the Web version of this article.)

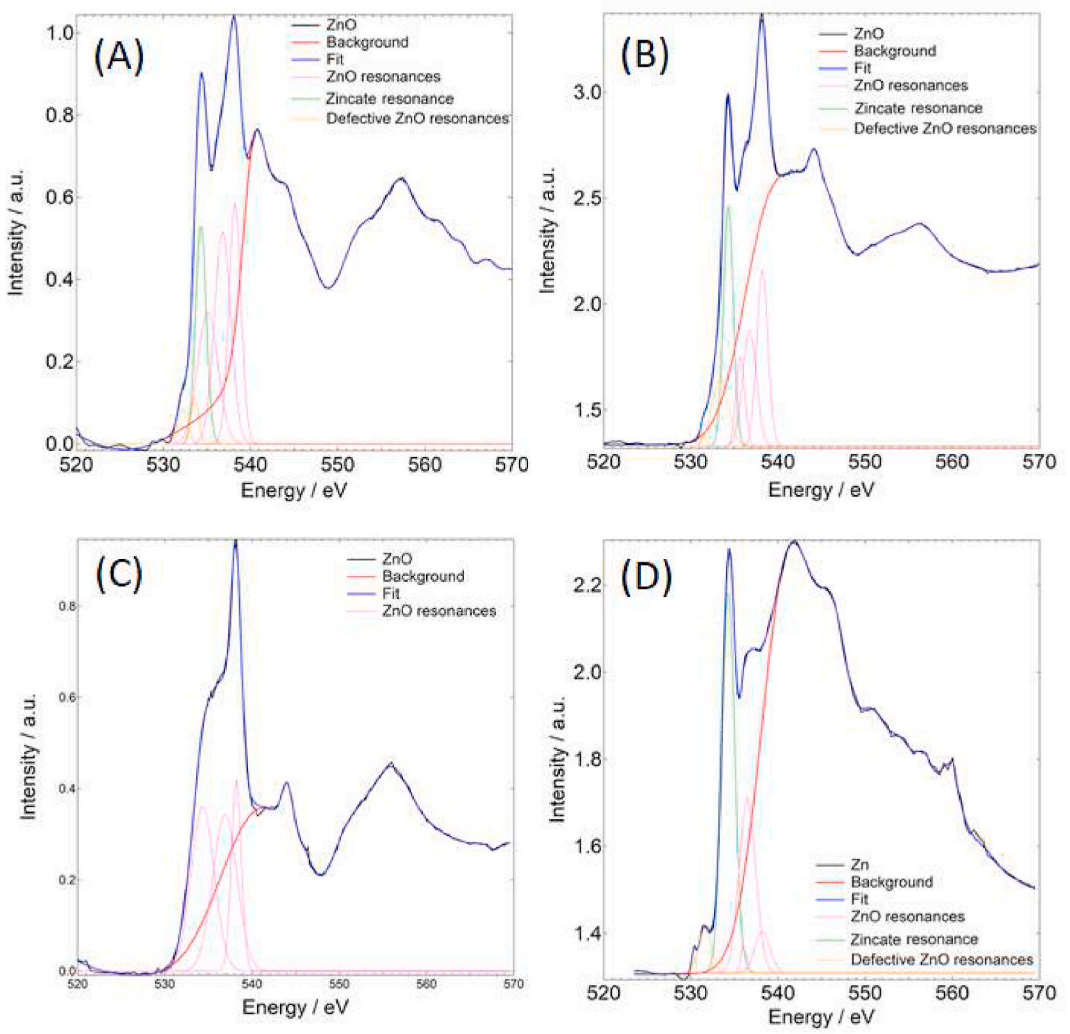

Fig. 5. O K-edge XAS spectra of: A) Zn electrode after discharge (condition A2), B) and C) ZnO electrode after application of single charge electrochemical polarization (condition B), D) ZnO electrode, after electrochemical cycling, terminated in charged state (condition C). The red and blue solid-lines indicate the background and the fit lines, respectively; the grayscale dashed-profiles indicate the different components for each species. (For interpretation of the references to colour in this figure legend, the reader is referred to the Web version of this article.)

band and their hybridization with Zn orbitals. Representative O K-edge XAS spectra of the oxide and zincate standards are shown in Fig. 3B and C. Due to the high sensitivity of the O K-edge spectra to the details of O chemistry, it was not possible to achieve accurate fitting with a linear combination using the spectra of the standards, as done for Zn L-edge spectra. Thus, we analysed the spectra by using a multi-gaussian fitting approach, along the lines described in Refs. [57,58]. The edge region of the standard ZnO spectrum in Fig. 3B was fitted as the sum of three components peaking at 533.8 eV, 536.1 eV and 538.2 eV. In particular, we considered, according to the literature [23,25,59], the peak at 538.2 eV as the principal component of the ZnO species, thus we kept this position fixed in each spectrum where ZnO is present. In the zincate standard spectrum in Fig. 3C, the characteristic zincate component is at 534.3 eV [54], together with the components associated with ZnO (535.5 eV, 536.7 eV and 538.2 eV) and defective ZnO (531.3 eV and 531.7 eV). Table 1 reports a summary of the Zn L-edge and O K-edge electronic transitions with the associated literature. The Zn XAS spectra of the standard samples were further used as a basis for linear combination fitting of the μ-XAS measured after electrode cycling steps.

Fig. 4 reports a selection of Zn L-edge μ-XAS, representative of dominant regions in the Zn L-edge maps of the electrode, measured in correspondence of the selected electrochemical conditions. We should point out that after the applied treatments, all Zn maps reveal inhomogeneity in the developed chemical state, as reported in detail in the next subsection. In the case of an initially metallic Zn electrode, subjected to deep discharge (condition A2, Fig. 4A), zincate-rich structures predominate with some presence of ZnO - estimated fractions: Zn-0; ZnO-0.1472; zincate-0.8528. In the case when the initially ZnO electrode is subjected to a single charge cycle (condition B, Fig. 4B and C) metallic Zn is formed, together with some zincate, resulting from the cathodic precipitation mentioned in Section 3.1, and residual ZnO. The varying local current densities in different locations, result in different quantities of reduced Zn, confirmed comparing the spectra in Fig. 4B (Zn-0.2638; ZnO-0.5764; zincate-0.2148) and Fig. 4C: (Zn-0.4181; ZnO-0.5965; zincate-0.1087). After a series of charge-discharge cycles, terminated in the charged state (condition C, Fig. 4D), zincate-enriched (Zn-0; ZnO-0.7042; zincate-0.2958) structures were found, with ZnO being the dominant species in the more heavily oxidized regions. Mixed ZnO/zincate states have been conjectured on the basis of indirect measurements [60] and in our direct spectroscopic observation we confirm their presence.

Fig. 5 shows the O K-edge μ-XAS extracted from dominant areas in the O K-edge maps, measured for samples subjected to the electrochemical treatments A, B and C, that are in general accordance with the Zn L-edge spectra: the features associated with ZnO, zincate and defective ZnO species can be identified. Specifically, the relative

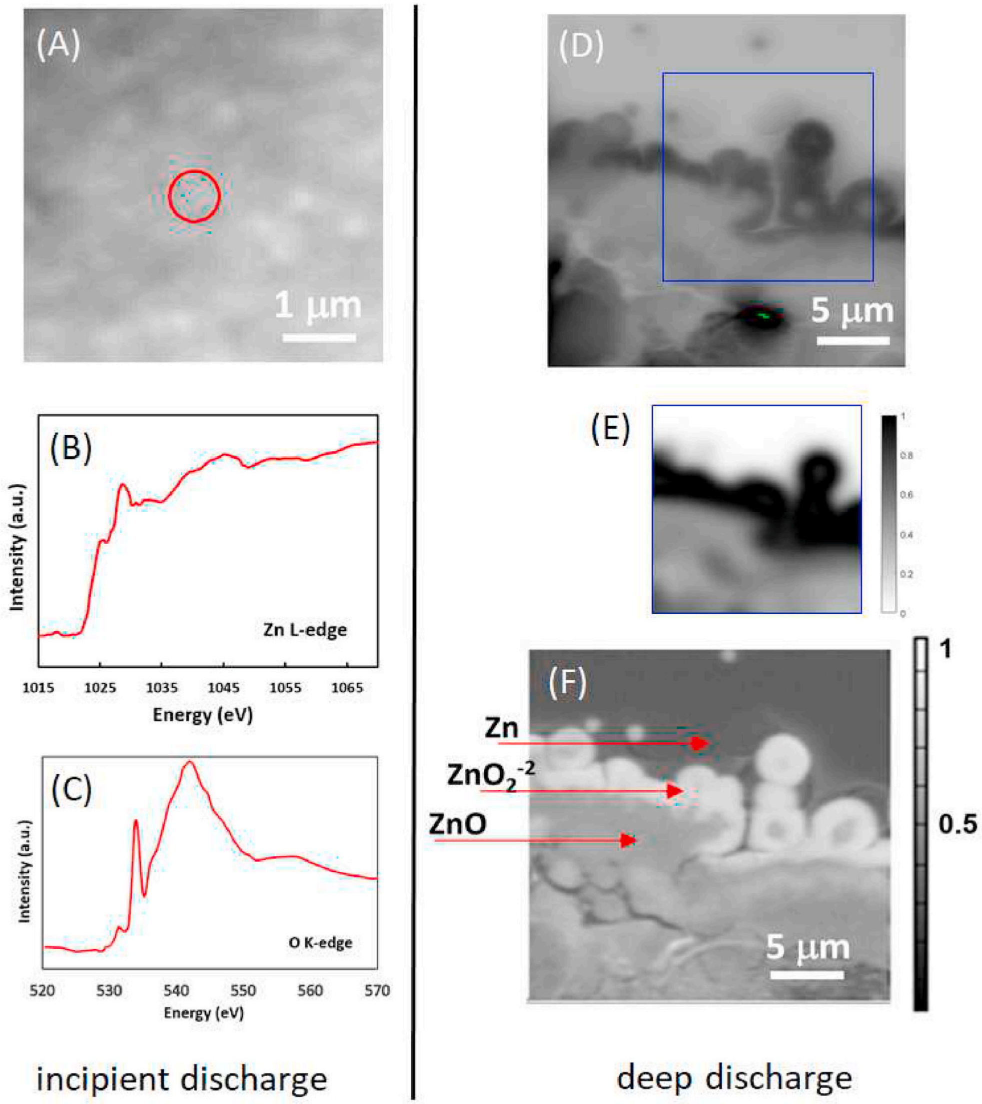

Fig. 6. Images and μ-XAS spectra of Zn electrode, subjected to incipient discharge (DOD ca. 12%, condition A1) and deep discharge (DOD ca. 60%, condition A2) at 1 mA cm^{-2}. (A) absorption and (4 D) transmission images taken at 1080 eV (above the Zn L-edge). (B) Zn L-edge XAS and (C) O K-edge XAS, measured in the microspot indicated of image (A). (E) Fit of the indicated region of map (D) with the DIB model: identified parameters, $B = 103.35 \pm 0.06$, $C = 2.8095 \pm 0.0075$. (F) Chemical-state map (differential map), based on a stack of absorption images at the Zn L-edge: the dominating species are indicated in the image.

intensities associated with the ZnO and zincate main peaks in Fig. 5D confirm the zincate enrichment due to the electrochemical treatment A2 (see Fig. 4A) and the ZnO predominance highlighted in Fig. 4D. Also the analysis of the O K-edge confirms the non-uniform distribution of oxides and zincates as a result of condition B, as discussed above. In fact, by inspection of the relative intensities of the ZnO and zincate main peaks in Fig. 5B, the coexistence of ZnO and zincate species in that area is confirmed, while the analysis of the spectrum in Fig. 5C confirms the predominance of ZnO species in another area of the same sample.

3.3.2. *X-ray absorption μ-XAS mapping*

In this Section, we report a selection of absorption and Zn L-edge maps, measured *ex situ* after the electrodes were subjected to electrochemical conditions A, B and C. All maps clearly reveal the developed heterogeneity in morphology and Zn chemical states.

The absorption, chemical maps and μ-XAS in Fig. 6 represent Zn electrodes subjected to incipient discharge (condition A1) and deep discharge (condition A2). The absorption image in Fig. 6A shows that under incipient discharge conditions the morphology is somewhat still preserved: the formation of submicron nodules of oxidized zinc, predominantly in the form of zincate, can be noticed, growing onto the metallic Zn film. Fig. 6D shows how deeper discharge leads to apparently new morphology, characterized by the growth of micrometric nodular structures, tending to coalesce, with ZnO cores surrounded by zincate shells. Zn oxidation under these conditions is compatible with a nucleation-and-growth phase formation mechanism, whereby precipitated zincate is the dominating species at the electrode-electrolyte interface, which tends to dehydrate to ZnO in the bulk. This scenario is consistent with the one suggested in Ref. [61], based on different vibrational and visible (linear and SHG) *in situ* spectro-electrochemical methods, but the novelty in the present study is that we jointly evidence the valence state and the spatial complexity.

The combination of submicrometer chemical and morphology mapping and micro-spectroscopy has allows us to associate the different types of Zn(II) with the morphology of the Zn passivation layers. Local differences in electronic (due to the formation of ZnO) and ionic (owing to zincate precipitation) conductivity at the electrode-electrolyte interface control the CD distribution at micrometric scale and determine the corrosion morphology that can be described quantitatively through the DIB model (Panel E). Remarkably accurate map fitting can be obtained with parameter values: $B = 103.35 \pm 0.06$, $C = 2.8095 \pm 0.0075$ (Frobenius error: 23%).

The images and μ-XAS spectra in Fig. 7 illustrate how the electrochemical reduction of a thin ZnO film results in the formation of a network of micro-sized Zn metal filaments (Panels (B-D, J, K)) on a background of residual, pristine ZnO (Panels (A, I)). The μ-XAS spectra (J) and (K) and chemical images (E-G) confirm that the presence of zincate correlates spatially with Zn metal. This seems to be a

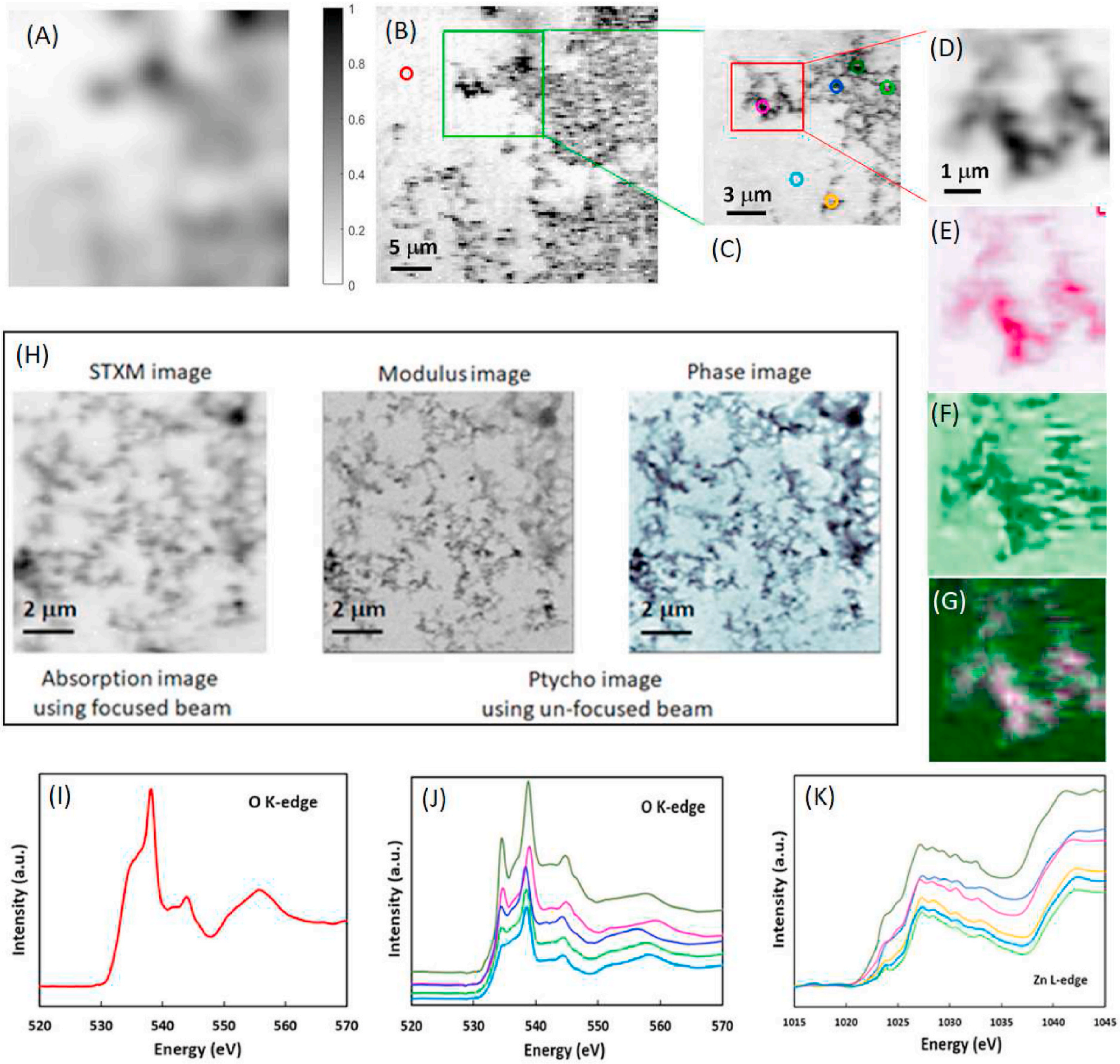

Fig. 7. Absorption images at O K-edge energy (B–D), O K-edge (I, J) and Zn L-edge (K) μ-XAS and chemical images (E–G) of ZnO electrode subjected to electrochemical reduction at −1 mA cm^{-2} to DOD ca. 44% (condition B). The absorption images (B–D) are measured above the O K-edge; (I) shows a typical O K-edge μ-XAS spectrum of a region where pristine ZnO dominates, indicated in image (1). (J, K) μ-XAS spectra are taken in the colour-coded locations indicated in image (C). (E–G) Chemical maps corresponding to the absorption image (D), taken at photon energies outlining the spectral feature with the predominant presence of zincates (E, red map) and zinc (F, green map). The RG (red-green) map (G) is an overlap illustrating the relative lateral distribution of these phases. (H) Demonstration of the gain in lateral resolution using ptychography, compared to SXM absorption imaging. The ptychographic images are obtained from diffraction images recorded using un-focused beam at the Zn L-edge with 10,000 iterations of the difference Map algorithm. (A) Fit of the map (B) with the DIB model: identified parameters, B = 96,444 ± 0.204, C = 2.7686 ± 0.0255. (For interpretation of the references to colour in this figure legend, the reader is referred to the Web version of this article.)

characteristic feature of Zn electrodeposition in a weakly acidic aqueous solution. It is also worth noting that ZnO is scarcely present in the region where Zn has formed. Again, good map fitting (Panel (A)) can be achieved with the DIB model with optimal parameters: B = 96,444 ± 0.204, C = 2.7686 ± 0.0255 (Frobenius error: 16%). Quantitative details of the relative contribution of catholyte alcalinization in high-CD locations and re-oxidation (self-discharge) in low-CD ones calls for future *in operando* studies, e.g. using cells like the ones we developed in Refs. [41,42]. *In operando* dynamic μ-XAS will also confirm that most likely the observed filamentary growth is controlled by the details of ZnO film granularity and defectivety. Further on, for increasing the space-resolution far below one micron, ptychography is an excellent choice [62–65]. The images reported in Panel (H) of Fig. 7, obtained at the I08-1 endstation, clearly confirm the notable gain in space resolution from 150 nm pixel size in the STXM micrograph to 10 nm in the reconstructed ptychography images, in addition to the availability of complementary modulus and phase contrast modes.

Fig. 8 reports absorption and chemical-state maps of a ZnO electrode, subjected to 10 charge-discharge cycles at ±1 mA cm^{-2} and terminated cathodically (condition C). The spectral information was handled in the same way as in Fig. 7. The morpho-chemistry of the cycled electrode is characterized by a Zn metal background with scattered, relatively thick crystallites, generally exhibiting protruding needle-shaped structures. Zn present in these crystallites is predominantly ZnO (Panel (G) of Fig. 8), while zincate seems to outline the surface of these features, in analogy with the core-shell structures observed in the oxidation experiment (condition A2, Fig. 6D–F).

The colocation of Zn and zincate, noted in the ZnO reduction experiment (condition B, Fig. 7), seem confirmed, even though less spatially defined as a result of accumulating redox cycles. Moreover, the

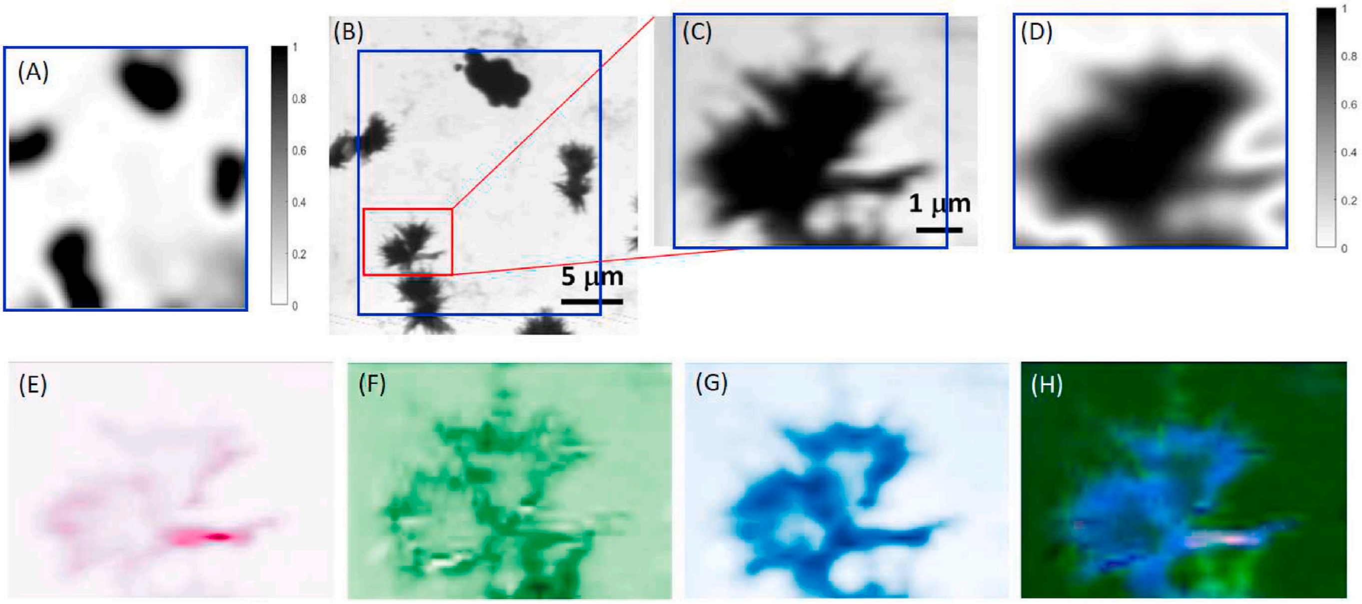

Fig. 8. Absorption and chemical maps of ZnO electrode subjected to 10 charge-discharge cycles at -1 mA cm^{-2} to DOD ca. 44% (condition B), terminated cathodically. (B, C) Absorption images taken above the O K-edge, (E–H) Chemical maps, indicating the location of predominating: zincates (E, red map), Zn (F, green map) and ZnO (G, blue map). The RGB (H, red-green-blue) map is an overlap illustrating the relative lateral distribution of these phases. (A, D) Fits of the indicated regions of maps (B) and (C) with the DIB model: identified parameters, respectively, B = 98.865 ± 0.028 (map (A), 98.890 ± 0.04 (map(D)); C = 2.796 ± 0.034 (map (A), 2.799 ± 0.049 (map (D))). (For interpretation of the references to colour in this figure legend, the reader is referred to the Web version of this article.)

ZnO spatial distribution clearly reveals that this is a secondary formation, resulting from electrochemical oxidation, and probably consolidated by incomplete reduction. Thus, the main characteristic of the chemical-state distribution developed from cycling, is its control by the formation of micrometric grains, chiefly consisting of ZnO. The grains tend to localize the electrochemical processes, increasing the CD at the edge of these structures, as witnessed by the needle shaped protrusion, that might play the role of dendrite precursors. The XAS maps are successfully fitted with the DIB model: noticeably, the low- and high-magnification maps (Panels (B, C) of Fig. 8) can be independently fitted with essentially the same set of parameters (Panels (A, D) of Fig. 8): B = 98.865 ± 0.028 (map (A), 98.890 ± 0.04 (map(D)); C = 2.796 ± 0.034 (map (A), 2.799 ± 0.049 (map (D))). (Frobenius errors: 40 and 21%).

Considering jointly the XAS maps fits corresponding to electrochemical conditions A, B and C (Figs. 6E, 7A and 8A, D), it can be noticed that the same values of parameter C are found in all cases, while different values of parameter B correspond to the different experiments. Specifically, B grows systematically going: (i) from charging (exclusively reduction, Fig. 7A): B = 96,444 ± 0.204; (ii) to charge-discharge cycling (alternated reduction and oxidation, Fig. 8A, D): B = 98.865 ± 0.028; and finally (iii) to deep discharge (exclusively oxidation, Fig. 6E): B = 103.35 ± 0.06. These results show that adsorption of electroactive species – modelled by parameter C [35,66] –, most probably zincates or reduction intermediates [67] essentially plays the same role in the electrochemical processes, leading to electrode structuring, taking place in the three investigated conditions, while the degree of inhibition that adsorbates causes to the faradaic process – modelled by parameter B [35,67] – is different in charge and discharge, while an intermediate value of B is coherently found in cycling experiments.

4. Conclusions

The present complementary electrochemical, X-ray imaging and micro-spectroscopy study, accompanied by mathematical modelling of XAS maps, has added lacking molecular-level information and physico-chemical rationalization on the nature and spatial distribution of the chemical state of Zn forming at the electrode/electrolyte interface as a result of cyclic electrochemical oxidation of Zn and reduction of Zn(II) species in weakly acidic aqueous electrolyte. The obtained results have outlined the role of parasitic phase formation in the buildup of locally passivating layers, that are strong candidates for the triggering of shape changes. The reported findings highlight the formation of zincates due to local alkalinization, followed by their precipitation due to transient, cathodic supersaturation and decomposition to ZnO. The evidenced generation of complex morpho-chemical patterns of the Zn electrode, with patches of different ionic and electronic conductivity, is clear evidence for cumulative localization of electrochemical oxidation and reduction rates. In fact, anodic conditions give rise to soluble and insoluble Zn(II) species - dictated by the local alkalinity developing during the cathodic cycle -, and the heterogeneous CD - influenced by the presence of insulating patches - can lead to direct formation of non-stoichiometric ZnO. Moreover, map fitting in the framework of the DIB mathematical model allowed to associate the heterogeneities developing at the Zn electrode surface with basic physico-chemical processes, highlighting the key role of the inhibition of faradaic processes brought about by the adsorption of electroactive species, that can be related to zincates. The findings in our studies provide clear evidence that current-density distributions that are nominally homogeneous on the electrode scale, can lead to mesoscopic heterogeneities that, in turn, end up controlling the nucleation distribution of new phases and the local deactivation of the electrode, finally leading to outgrowth in selected regions.

These conclusions point towards one main direction of further development: the knowledge-based use of additives. This approach is commonplace in the literature, but it seems not to have led to the same success achieved in metal plating. The present results and cognate work in our group [46,68] suggest that the reason is probably that the synergy between anodic and cathodic conditions has to be explicitly addressed. This situation calls for molecular-level understanding of the role of additives not only under cathodic and anodic conditions separately, but also in common, exploiting the cathodic impact of anodically formed phases and *vice versa*.

CRediT authorship contribution statement

Majid Kazemian: Conceptualization, Methodology, Software, Validation, Formal analysis, Investigation, Resources, Data curation, Writing – original draft, Writing – review & editing, Visualization, Project administration, Funding acquisition. **Francesca Rossi:** Methodology, Software, Validation, Formal analysis, Investigation, Data curation, Writing – original draft, Writing – review & editing, Visualization. **Andrea Casaroli:** Methodology, Validation, Investigation, Data curation, Visualization. **Tommaso Caielli:** Validation, Investigation, Data curation, Visualization. **Burkhard Kaulich:** Conceptualization, Methodology, Investigation, Formal analysis, Resources, Writing – review & editing. **Maya Kiskinova:** Conceptualization, Methodology, Validation, Formal analysis, Investigation, Resources, Data curation, Writing – original draft, Writing – review & editing, Visualization. **Ivonne Sgura:** Methodology, Software, Validation, Formal analysis, Data curation, Writing – review & editing, Visualization. **Benedetto Bozzini:** Conceptualization, Methodology, Software, Validation, Formal analysis, Investigation, Resources, Data curation, Writing – original draft, Writing – review & editing, Visualization, Project administration, Funding acquisition.

Declaration of competing interest

The authors declare that they have no known competing financial interests or personal relationships that could have appeared to influence the work reported in this paper.

Acknowledgements

The SXM measurements at I08 beamline and sample materials were performed at Diamond Light Source Ltd. [beam time MG22398-1]. Sample preparation in the Nanofabrication Facility at the University of Bath was supported by the EPSRC ‘Access to Nanolithography’ programme (grant ref. EP/K040324/1). We thank Dr. Chiara Negri (Politecnico di Milano) for the useful discussions on the data analysis of the XAS O K-edge spectra.

References

[1] European Environment Agency, Trends and Projections in Europe 2019 - Tracking Progress towards Europes Climate and Energy Targets —, European Environment Agency, 2019. https://www.eea.europa.eu//publications/trends-and-projections-in-europe-1.
[2] Y. Shi, Y. Chen, L. Shi, K. Wang, B. Wang, L. Li, Y. Ma, Y. Li, Z. Sun, W. Ali, S. Ding, An overview and future perspectives of rechargeable zinc batteries, Small 16 (2020) 1–28, https://doi.org/10.1002/smll.202000730.
[3] Y. Zhang, Z. Chen, H. Qiu, W. Yang, Z. Zhao, J. Zhao, G. Cui, Pursuit of reversible Zn electrochemistry: a time-honored challenge towards low-cost and green energy storage, NPG Asia Mater. 12 (2020) 1–24, https://doi.org/10.1038/s41427-019-0167-1.
[4] J. Shin, J. Lee, Y. Park, J.W. Choi, Aqueous zinc ion batteries: focus on zinc metal anodes, Chem. Sci. 11 (2020) 2028–2044, https://doi.org/10.1039/d0sc00022a.
[5] P. Keil, S.F. Schuster, J. Wilhelm, J. Travi, A. Hauser, R.C. Karl, A. Jossen, Calendar aging of lithium-ion batteries, J. Electrochem. Soc. 163 (2016) A1872–A1880, https://doi.org/10.1149/2.0411609jes.
[6] N. Zhang, X. Chen, M. Yu, Z. Niu, F. Cheng, J. Chen, Materials chemistry for rechargeable zinc-ion batteries, Chem. Soc. Rev. 49 (2020) 4203–4219, https://doi.org/10.1039/c9cs00349e.
[7] D. Yang, H. Tan, X. Rui, Y. Yu, Electrode materials for rechargeable zinc-ion and zinc-air batteries: current status and future perspectives, Electrochem. Energy Rev. 2 (2019) 395–427, https://doi.org/10.1007/s41918-019-00035-5.
[8] T.S. Lee, Hydrogen over potential on pure metals in alkaline solution, J. Electrochem. Soc. 118 (1971) 1278, https://doi.org/10.1149/1.2408305.
[9] Y. Sawada, Transition of growth form from dendrite to aggregate, Phys. A Stat. Mech. Its Appl. 140 (1986) 134–141, https://doi.org/10.1016/0378-4371(86)90213-X.
[10] A.R. Despic, J. Diggle, J.O. Bockris, Mechanism of the formation of zinc dendrites, J. Electrochem. Soc. 115 (1968) 507, https://doi.org/10.1149/1.2411297.
[11] C. Cachet, U. Ströder, R. Wiart, The kinetics of zinc electrode in alkaline zincate electrolytes, Electrochim. Acta 27 (1982) 903–908, https://doi.org/10.1016/0013-4686(82)80214-4.
[12] T. Yamamoto, T. Shoji, Rechargeable ZnlZnSOlMnO2-type cells, Inorg. Chim. Acta. 117 (1986) L27–L28, https://doi.org/10.1016/S0020-1693(00)82175-1.
[13] J. Hao, X. Li, X. Zeng, D. Li, J. Mao, Z. Guo, Deeply understanding the Zn anode behaviour and corresponding improvement strategies in different aqueous Zn-based batteries, Energy Environ. Sci. 13 (2020) 3917–3949, https://doi.org/10.1039/d0ee02162h.
[14] H. Glatz, E. Tervoort, D. Kundu, Unveiling critical insight into the Zn metal anode cyclability in mildly acidic aqueous electrolytes: implications for aqueous zinc batteries, ACS Appl. Mater. Interfaces 12 (2020) 3522–3530, https://doi.org/10.1021/acsami.9b16125.
[15] N. Zhang, F. Cheng, Y. Liu, Q. Zhao, K. Lei, C. Chen, X. Liu, J. Chen, Cation-deficient spinel ZnMn2O4 cathode in Zn(CF3SO3)2 electrolyte for rechargeable aqueous Zn-ion battery, J. Am. Chem. Soc. 138 (2016) 12894–12901, https://doi.org/10.1021/jacs.6b05958.
[16] H. Pan, Y. Shao, P. Yan, Y. Cheng, K.S. Han, Z. Nie, C. Wang, J. Yang, X. Li, P. Bhattacharya, K.T. Mueller, J. Liu, Reversible aqueous zinc/manganese oxide energy storage from conversion reactions, Nat. Energy 1 (2016) 16039, https://doi.org/10.1038/nenergy.2016.39.
[17] N. Alias, A.A. Mohamad, Morphology study of electrodeposited zinc from zinc sulfate solutions as anode for zinc-air and zinc-carbon batteries, J. King Saud Univ. - Eng. Sci. 27 (2015) 43–48, https://doi.org/10.1016/j.jksues.2013.03.003.
[18] Z. Liu, T. Cui, G. Pulletikurthi, A. Lahiri, T. Carstens, M. Olschewski, F. Endres, Dendrite-free nanocrystalline zinc electrodeposition from an ionic liquid containing nickel triflate for rechargeable Zn-based batteries, Angew. Chem. Int. Ed. 55 (2016) 2889–2893, https://doi.org/10.1002/anie.201509364.
[19] B.S. Lee, S. Cui, X. Xing, H. Liu, X. Yue, V. Petrova, H.D. Lim, R. Chen, P. Liu, Dendrite suppression membranes for rechargeable zinc batteries, ACS Appl. Mater. Interfaces 10 (2018) 38928–38935, https://doi.org/10.1021/acsami.8b14022.
[20] A. Bayaguud, X. Luo, Y. Fu, C. Zhu, Cationic surfactant-type electrolyte additive enables three-dimensional dendrite-free zinc anode for stable zinc-ion batteries, ACS Energy Lett. 5 (2020) 3012–3020, https://doi.org/10.1021/acsenergylett.0c01792.
[21] M. Cui, Y. Xiao, L. Kang, W. Du, Y. Gao, X. Sun, Y. Zhou, X. Li, H. Li, F. Jiang, C. Zhi, Quasi-isolated Au particles as heterogeneous seeds to guide uniform Zn deposition for aqueous zinc-ion batteries, ACS Appl. Energy Mater. 2 (2019) 6490–6496, https://doi.org/10.1021/acsaem.9b01063.
[22] C.J. Pelliccione, Y. Ding, E.V. Timofeeva, C.U. Segre, In situ XAFS study of the capacity fading mechanisms in ZnO anodes for lithium-ion batteries, J. Electrochem. Soc. 162 (2015) A1935–A1939, https://doi.org/10.1149/2.1011509jes.
[23] M. Petravic, R. Peter, M. Varasanec, Y. Yang, M. Yano, K. Koike, Hydrogen in ZnO : X-ray absorption measurements and multiple scattering theory, 2014, pp. 60–63.
[24] C.L. Dong, C. Persson, L. Vayssieres, A. Augustsson, T. Schmitt, M. Mattesini, R. Ahuja, C.L. Chang, J. Guo, Electronic structure of nanostructured ZnO from x-ray absorption and emission spectroscopy and the local density approximation, 195325, 2–6, https://doi.org/10.1103/PhysRevB.70.195325, 2004.
[25] A.K. Yadav, S.M. Haque, S. Tripathi, D. Shukla, A. Ahmed, D.M. Phase, S. Bandyopadhyay, S.N. Jha, D. Bhattacharyya, RSC Advances Investigation of Fe doped ZnO thin fi lms by X-ray absorption spectroscopy. https://doi.org/10.1039/c6ra07195c, 2016, 74982-74990.
[26] J.F. Parker, J.S. Ko, D.R. Rolison, J.W. Long, Translating materials-level performance into device-relevant metrics for zinc-baser batteries, Joule 2 (2018) 2519–2527, https://doi.org/10.1016/j.joule.2018.11.007.
[27] B. Bozzini, A. Gianoncelli, C. Mele, I. Sgura, M. Kiskinova, Electrodeposition of a Mn–Cu–ZnO hybrid material for supercapacitors: a soft X-ray fluorescence and absorption microspectroscopy study, Chemelectrochem 1 (2014) 392–399, https://doi.org/10.1002/celc.201300099.
[28] A. Gianoncelli, B. Kaulich, M. Kiskinova, C. Mele, M. Prasciolu, I. Sgura, B. Bozzini, Fabrication and testing of an electrochemical microcell for in situ soft X-ray microspectroscopy measurements, J. Phys. Conf. Ser. 425 (2013), 182010, https://doi.org/10.1088/1742-6596/425/18/182010.
[29] B. Bozzini, A. Gianoncelli, B. Kaulich, M. Kiskinova, M. Prasciolu, I. Sgura, Metallic plate corrosion and uptake of corrosion products by nafion in polymer electrolyte membrane fuel cells, ChemSusChem 3 (2010) 846–850, https://doi.org/10.1002/cssc.201000048.
[30] B. Bozzini, L. D'Urzo, A. Gianoncelli, B. Kaulich, M. Prasciolu, I. Sgura, E. Tondo, M. Kiskinova, An in situ synchrotron-based soft X-ray microscopy investigation of Ni electrodeposition in a thin-layer cell, J. Phys. Chem. C 113 (2009) 9783–9787, https://doi.org/10.1021/jp901528g.
[31] M. Caglar, S. Ilican, Y. Caglar, F. Yakuphanoglu, Electrical conductivity and optical properties of ZnO nanostructured thin film, Appl. Surf. Sci. 255 (2009) 4491–4496, https://doi.org/10.1016/j.apsusc.2008.11.055.
[32] W. Wu, S. Shabhag, J. Chang, A. Rutt, J.F. Whitacre, Relating electrolyte concentration to performance and stability for NaTi 2 (PO 4) 3/Na 0.44 MnO 2 aqueous sodium-ion batteries, J. Electrochem. Soc. 162 (2015) A803–A808, https://doi.org/10.1149/2.0121506jes.
[33] M.K. Abyaneh, T. Araki, B. Kaulich, A sub-microanalysis approach in chemical characterisation of gold nanorods formed by a novel polymer-immobilised gold seeds base, Nanomaterials 7 (2017), https://doi.org/10.3390/nano7100331.
[34] M. Lerotic, 2nd Lookd Consulting, (n.d.). https://2ndlookconsulting.com/.
[35] B. Bozzini, D. Lacitignola, I. Sgura, Spatio-temporal organization in alloy electrodeposition: a morphochemical mathematical model and its experimental validation, J. Solid State Electrochem. 17 (2013) 467–479, https://doi.org/10.1007/s10008-012-1945-7.
[36] D. Lacitignola, B. Bozzini, I. Sgura, Spatio-temporal organization in a morphochemical electrodeposition model: hopf and Turing instabilities and their interplay, Eur. J. Appl. Math. 26 (2015) 143–173, https://doi.org/10.1017/S0956792514000370.

[37] I. Sgura, A.S. Lawless, B. Bozzini, Parameter estimation for a morphochemical reaction-diffusion model of electrochemical pattern formation, Inverse Probl. Sci. Eng. 27 (2019) 618–647, https://doi.org/10.1080/17415977.2018.1490278.

[38] I. Sgura, B. Bozzini, XRF map identification problems based on a PDE electrodeposition model, J. Phys. D. 50 (2017), 154002, https://doi.org/10.1088/1361-6463/aa5a1f (21 pages).

[39] B. Bozzini, M. Amati, Ts Dobrovolska, L. Gregoratti, I. Krastev, I. Sgura, A. Taurino, M. Kiskinova, Depth-dependent scanning photoelectron microspectroscopy unravels the mechanism of dynamic pattern formation in alloy electrodeposition, J. Phys. Chem. C 112 (2018) 15996–16007, https://doi.org/10.1021/acs.jpcc.8b01267.

[40] B. Bozzini, A. Gianoncelli, G. Kourousias, M. Boniardi, A. Casaroli, S. Dal Zilio, R. Hussain, M.K. Abyaneh, M. Kiskinova, C. Mele, S. Tedeschi, G. Pietro De Gaudenzi, The role of chromium in the corrosion performance of cobalt- and cobalt-nickel based hardmetal binders: a study centred on X-ray absorption microspectroscopy, Int. J. Refract. Metals Hard Mater. 92 (2020), 105320, https://doi.org/10.1016/j.ijrmhm.2020.105320.

[41] B. Bozzini, M. Kazemian, M. Kiskinova, G. Kourousias, C. Mele, A. Gianoncelli, Operando soft X-ray microscope study of rechargeable Zn–air battery anodes in deep eutectic solvent electrolyte, X Ray Spectrom. 48 (2019) 527–535, https://doi.org/10.1002/xrs.3031.

[42] B. Bozzini, A. Gianoncelli, P. Bocchetta, S. Dal Zilio, G. Kourousias, Fabrication of a sealed electrochemical microcell for in situ soft X-ray microspectroscopy and testing with in situ Co-polypyrrole composite electrodeposition for Pt-free oxygen electrocatalysis, Anal. Chem. 86 (2014) 664–670, https://doi.org/10.1021/ac403004v.

[43] M. Schlesinger, M. Paunovic, Modern Electroplating, Fifth Edition, J. Wiley and Sons, Inc.,, Hoboke, New Jersey, 2010, p. 210.

[44] C. Cachet, F. Ganne, S. Joiret, G. Maurin, J. Petitjean, V. Vivier, R. Wiart, EIS investigation of zinc dissolution in aerated sulphate medium. Part II: zinc coatings, Electrochim. Acta 47 (2002) 3409–3422, https://doi.org/10.1016/S0013-4686(02)00277-3.

[45] C. Mele, A. Bilotta, P. Bocchetta, B. Bozzini, Characterization of the particulate anode of a laboratory flow Zn–air fuel cell, J. Appl. Electrochem. 47 (2017) 877–888, https://doi.org/10.1007/s10800-017-1088-8.

[46] F. Rossi, L. Mancini, I. Sgura, M. Boniardi, A. Casaroli, A.P. Kao, B. Bozzini, Insight into the Cycling Behaviour of Metal Anodes, Enabled by X-Ray Tomography and Mathematical Modelling, ChemElectroChem, Submitted.

[47] K. Saber, C.C. Koch, P.S. Fedkiw, Pulse current electrodeposition of nanocrystalline zinc, Mater. Sci. Eng. 341 (2003) 174–181, https://doi.org/10.1016/S0921-5093(02)00198-3.

[48] N. Alias, A.A. Mohamad, Morphology study of electrodeposited zinc from zinc sulfate solutions as anode for zinc-air and zinc-carbon batteries, J. King Saud Univ. - Eng. Sci. 27 (2015) 43–48, https://doi.org/10.1016/j.jksues.2013.03.003.

[49] K. Raeissi, A. Saatchi, M.A. Golozar, Effect of nucleation mode on the morphology and texture of electrodeposited zinc, J. Appl. Electrochem. 33 (2003) 635–642, https://doi.org/10.1023/A:1024914503902.

[50] L.E. Blanc, D. Kundu, L.F. Nazar, Scientific challenges for the implementation of Zn-ion batteries, Joule 4 (2020) 771–779, https://doi.org/10.1016/j.joule.2020.03.002.

[51] B. Bozzini, F. Rossi, S. Bacheri, M. Boniardi, C. Mele, A Parametric Study of Zn-Air Fuel Cell Polarization Curves, Electrochim. Acta. Submitted (n.d.).

[52] J. Sahu, S. Soni, S. Kumar, B. Dalela, P.A. Alvi, S.S. Sharma, D.M. Phase, M. Gupta, S. Kumar, S. Dalela, Defects and oxygen vacancies tailored structural, optical and electronic structure properties of Co-doped ZnO nanoparticle samples probed using soft X-ray absorption spectroscopy, Vacuum 179 (2020), 109538, https://doi.org/10.1016/j.vacuum.2020.109538.

[53] R. Bhardwaj, A. Bharti, J.P. Singh, K.H. Chae, N. Goyal, S. Gautam, Structural and electronic investigation of ZnO nanostructures synthesized under different environments, Heliyon 4 (2018), e00594, https://doi.org/10.1016/j.heliyon.2018.e00594.

[54] N. Kıcır, O.M. Ozkendir, A.H. Farha, F. Kırmızıgül, T. Tuken, C. Gumus, S. Çabuk, M. Erbil, Y. Ufuktepe, Physical and electronic properties of electrodeposited ZnO thin films: dependence on thickness, Indian J. Phys. 89 (2015) 1013–1023, https://doi.org/10.1007/s12648-015-0675-y.

[55] J.W. Chiou, J.C. Jan, H.M. Tsai, C.W. Bao, W.F. Pong, M.H. Tsai, I.H. Hong, R. Klauser, J.F. Lee, J.J. Wu, S.C. Liu, Electronic structure of ZnO nanorods studied by angle-dependent X-ray absorption spectroscopy and scanning photoelectron microscopy, Appl. Phys. Lett. 84 (2004) 3462–3464, https://doi.org/10.1063/1.1737075.

[56] O.M. Ozkendir, S. Yildirimcan, A. Yuzer, K. Ocakoglu, Crystal and electronic structure study of Mn doped wurtzite ZnO nanoparticles, Prog. Nat. Sci. Mater. Int. 26 (2016) 347–353, https://doi.org/10.1016/j.pnsc.2016.07.004.

[57] S. Agrestini, S. Sanna, K. Zheng, R. De Renzi, E. Pusceddu, G. Concas, N.L. Saini, A. Bianconi, Soft x-ray absorption and high-resolution powder x-ray diffraction study of superconducting CaxLa1-xBa1.75-xLa 0.25+xCu3Oy system, J. Phys. Chem. Solid. 75 (2014) 259–264, https://doi.org/10.1016/j.jpcs.2013.09.026.

[58] M. Risch, K.A. Stoerzinger, B. Han, T.Z. Regier, D. Peak, S.Y. Sayed, C. Wei, Z. Xu, Y. Shao-Horn, Redox processes of manganese oxide in catalyzing oxygen evolution and reduction: an in situ soft X-ray absorption spectroscopy study, J. Phys. Chem. C 121 (2017) 17682–17692, https://doi.org/10.1021/acs.jpcc.7b05592.

[59] W. Dong, J.L. Shi, T.S. Wang, Y.X. Yin, C.R. Wang, Y.G. Guo, 3D zinc@carbon fiber composite framework anode for aqueous Zn-MnO2 batteries, RSC Adv. 8 (2018) 19157–19163, https://doi.org/10.1039/c8ra03226b.

[60] T. Arlt, D. Schröder, U. Krewer, I. Manke, In operando monitoring of the state of charge and species distribution in zinc air batteries using X-ray tomography and model-based simulations, Phys. Chem. Chem. Phys. 16 (2014) 22273–22280, https://doi.org/10.1039/C4CP02878C.

[61] C. Mele, B. Bozzini, Spectroelectrochemical investigation of the anodic and cathodic behaviour of zinc in 5.3 M KOH, J. Appl. Electrochem. 45 (2015) 43–50, https://doi.org/10.1007/s10800-014-0755-2.

[62] G. Kourousias, B. Bozzini, M.W.M. Jones, G.A. Van Riessen, S. Dal Zilio, F. Billè, M. Kiskinova, A. Gianoncelli, Monitoring dynamic electrochemical processes with in situ ptychography, Appl. Nanosci. 8 (2018) 627–636, https://doi.org/10.1007/s13204-018-0703-2.

[63] G. Kourousias, B. Bozzini, A. Gianoncelli, M.W.M. Jones, M. Junker, G. van Riessen, M. Kiskinova, Shedding light on electrodeposition dynamics tracked in situ via soft X-ray coherent diffraction imaging, Nano Res. 9 (2016) 2046–2056, https://doi.org/10.1007/s12274-016-1095-9.

[64] B. Bozzini, G. Kourousias, A. Gianoncelli, M.W.M. Jones, G. Van Riessen, M. Kiskinova, Soft X-ray ptychography as a tool for in operando morphochemical studies of electrodeposition processes with nanometric lateral resolution, J. Electron. Spectrosc. Relat. Phenom. 220 (2017) 147–155, https://doi.org/10.1016/j.elspec.2017.01.004.

[65] B. Bozzini, G. Kourousias, A. Gianoncelli, In situ observation of dynamic electrodeposition processes by soft x-ray fluorescence microspectroscopy and keyhole coherent diffractive imaging, J. Phys. D Appl. Phys. 50 (2017), 124001, https://doi.org/10.1088/1361-6463/aa57a2.

[66] D. Lacitignola, I. Sgura, B. Bozzini, Ts Dobrovolska, I. Krastev, Spiral waves on the sphere for an alloy electrodeposition model, Commun. Nonlinear Sci. Numer. Simulat. 79 (2019), 104930, https://doi.org/10.1016/j.cnsns.2019.104930, 14 pages.

[67] D. Lacitignola, B. Bozzini, M. Frittelli, I. Sgura, Turing pattern formation on the sphere for a morphochemical reaction-diffusion model for electrodeposition, Commun. Nonlinear Sci. Numer. Simulat. 48 (2017) 484–508, https://doi.org/10.1016/j.cnsns.2017.01.008.

[68] B. Bozzini, F. Rossi, C. Mele, M. Boniardi, Electrodeposition of Zn from alkaline electrolytes containing quaternary ammonium salts and ionomers: the impact of cathodic-anodic cycling conditions, Chemelectrochem (2020), https://doi.org/10.1002/celc.202000165 celc.202000165.